



COSMIC Variance in Binary Population Synthesis

Katelyn Breivik¹, Scott Coughlin^{2,3,4}, Michael Zevin^{2,3}, Carl L. Rodriguez⁵, Kyle Kremer^{2,3}, Claire S. Ye^{2,3},
Jeff J. Andrews^{2,3,6}, Michael Kurkowski^{2,7}, Matthew C. Digman⁸, Shane L. Larson^{2,3}, and Frederic A. Rasio^{2,3}

¹ Canadian Institute for Theoretical Astrophysics, University of Toronto, 60 St. George Street, Toronto, Ontario, M5S 1A7, Canada; kbreivik@cita.utoronto.ca

² Center for Interdisciplinary Exploration and Research in Astrophysics (CIERA), Northwestern University, 1800 Sherman Road, Evanston, IL 60201, USA

³ Department of Physics and Astronomy, Northwestern University, 2145 Sheridan Road, Evanston, IL 60208, USA

⁴ Physics and Astronomy, Cardiff University, Cardiff, CF10 2FH, UK

⁵ Harvard Institute for Theory and Computation, 60 Garden Street, Cambridge, MA 02138, USA

⁶ Niels Bohr Institute, University of Copenhagen, Blegdamsvej 17, DK-2100 Copenhagen, Denmark

⁷ Department of Physics, University of Notre Dame, 225 Nieuwland Science Hall, Notre Dame, IN 46556, USA

⁸ Center for Cosmology and AstroParticle Physics (CCAPP), Ohio State University, Columbus, OH 43210, USA

Received 2019 December 4; revised 2020 May 25; accepted 2020 June 15; published 2020 July 24

Abstract

The formation and evolution of binary stars are critical components of several fields in astronomy. The most numerous sources for gravitational wave observatories are inspiraling or merging compact binaries, while binary stars are present in nearly every electromagnetic survey regardless of the target population. Simulations of large binary populations serve to both predict and inform observations of electromagnetic and gravitational wave sources. Binary population synthesis is a tool that balances physical modeling with simulation speed to produce large binary populations on timescales of days. We present a community-developed binary population synthesis suite, COSMIC, which is designed to simulate compact-object binary populations and their progenitors. As a proof of concept, we simulate the Galactic population of compact binaries and their gravitational wave signals observable by the Laser Interferometer Space Antenna.

Unified Astronomy Thesaurus concepts: Compact binary stars (283); Interacting binary stars (801); Stellar populations (1622); Gravitational wave astronomy (675)

1. Introduction

Binary stars play a critical role, either as a signal or noise source, in nearly all fields of astronomy (Price-Whelan et al. 2019). Binary systems containing stellar remnants are the most prolific sources for both ground- and space-based gravitational wave (GW) observatories. The Laser Interferometer Gravitational Wave Observatory and Virgo (LIGO/Virgo) have detected the inspiral and merger of 10 binary black holes (BHs) and one binary neutron star (BNS; Abbott et al. 2019). The Laser Interferometer Space Antenna (LISA) is expected to observe the population of $\sim 10^7$ binary stellar remnants, or compact binaries, in the Milky Way and its surrounding environment forming a confusion foreground of gravitational radiation in the millihertz region of the GW spectrum. Tens of thousands of compact binaries, dominated in number by double white dwarfs (DWDs), are expected to be resolved above the foreground, offering a unique probe of the populations of stellar remnants in the local universe (e.g., Nelemans et al. 2001a; Ruiter et al. 2010; Yu & Jeffery 2010, 2015; Nisanke et al. 2012; Littenberg et al. 2013; Korol et al. 2017; Lamberts et al. 2018, 2019).

Simulations of compact-object binary populations are useful tools that enable astrophysical interpretations of GW sources and their progenitors. Binary population synthesis (BPS) combines single-star evolution with prescriptions for binary interactions to simulate binary populations from zero-age main sequence (ZAMS) through to the stellar-remnant phase. Generally, each BPS study seeks to determine which physical processes are most important in shaping observed catalog sources. To this end, in each study, a single population and its detection catalog are simulated for a single model or a set of several models that canvass the available parameter space.

Several BPS codes are currently in use, each with their own simulation techniques and focuses. This type of simulation originated with the work of Whyte & Eggleton (1985) and was soon followed by several BPS studies (e.g., Dewey & Cordes 1987; Lipunov & Postnov 1987; de Kool 1990; Hills et al. 1990; Ritter et al. 1991). BPS methods have since been iterated upon and widely applied to study many different binary populations of interest. One approach is to modify a stellar evolution code previously developed for single stars to include the effects of binary evolution, as found in *ev/STARS/TWIN* (Pols et al. 1995; Nelson & Eggleton 2001), the Brussels population number synthesis code (PNS, de Donder & Vanbeveren 2004), *BINSTAR* (Siess et al. 2013), *MESA* (Paxton et al. 2011, 2013, 2015, 2018, 2019), or *BPASS* (Eldridge & Stanway 2016; Stanway et al. 2016; Eldridge et al. 2017; Stanway & Eldridge 2018). Another approach is to generate large libraries of lookup tables for single stars and then use interpolation combined with simple binary evolution prescriptions, as done in *SEVN* (Spera et al. 2015; Spera & Mapelli 2017; Spera et al. 2019) or *COMBINE* (Kruckow et al. 2018).

The most widely applied technique is to use fitting formulae derived from single-star evolution models, which vary as a function of stellar age, mass, and metallicity. For example, Hurley et al. (2000) developed such a formalism based on the stellar evolution models of Pols et al. (1998). Different binary evolution prescriptions are applied to these fitting formulae to develop BPS codes, such as *Scenario Machine* (Lipunov et al. 1996a, 1996b, 2009), *IBiS* (Tutukov & Yungelson 1996, and references therein), *BSE* (Hurley et al. 2002), *SeBa* (Portegies Zwart & Verbunt 1996; Nelemans et al. 2001a; Toonen et al. 2012), *StarTrack* (Belczynski et al. 2002, 2008), *binary_c* (Izzard et al. 2004, 2006, 2009), *COMPAS* (Stevenson et al.

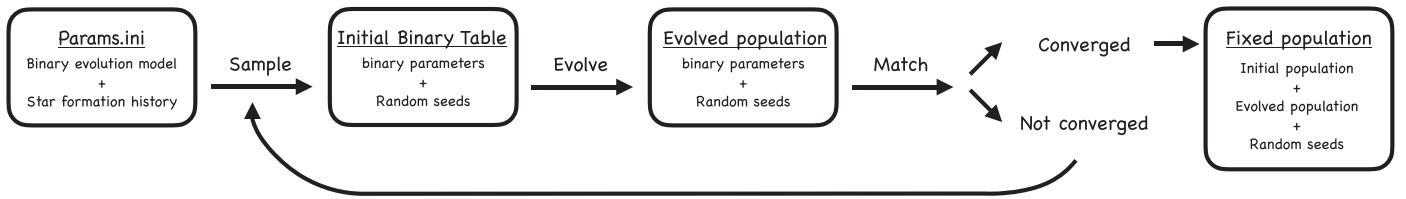


Figure 1. Schematic for the process COSMIC uses to generate a fixed population. Generally, the process moves from left to right. All quantities in the boxes are produced and available to the user, while all arrows represent modules within COSMIC that facilitate the evolution process. For a discussion of the match and convergence, see Section 2.1.2. See also the list of steps outlined in Section 2.

2017; Barrett et al. 2018), and MOBSE (Giacobbo & Mapelli 2018; Giacobbo et al. 2018). Given the wide variety of available software, studies like the POPCORN project, which compared the outputs of SeBa, StarTrack, binary_c, and the Brussels PNS code, are an invaluable resource that quantify theoretical uncertainties and confirm results across BPS software (Toonen et al. 2014). More recent population synthesis tools that use Markov Chain Monte Carlo methods (dart_board; Andrews et al. 2018), Gaussian processes (Barrett et al. 2017; Taylor & Gerosa 2018), or Adaptive Importance Sampling (STROOPWAFEL; Broekgaarden et al. 2019) are also available to provide better statistical descriptions of binary populations.

Here we present COSMIC (Compact Object Synthesis and Monte Carlo Investigation Code), a BPS code adapted from BSE that generates large binary populations that can be convolved with star formation history (SFH) and spatial distribution models to produce astrophysical realizations of binary populations.

Simulated detection catalogs from these astrophysical realizations can then inform the range of possible compact-object binary populations detectable with both GW or electromagnetic observations. The ability to generate a statistical sample of binary populations is especially important when considering populations with low numbers. For example, the subset of mass-transferring DWDs with helium accretors observable by LISA and Gaia is expected to contain *dozens* of systems, which are a tiny subset of the tens of thousands of DWDs individually detectable by LISA (Kremer et al. 2017; Breivik et al. 2018).

The paper is organized as follows. In Section 2 we summarize the key features of COSMIC. We detail the additional binary evolution prescriptions included in COSMIC beyond those contained in the original version of BSE in Section 3. In Section 4 we demonstrate the capabilities of COSMIC to produce a reference population of compact binaries observable by LISA, and we finish with conclusions in Section 5.

2. Overview: COSMIC

COSMIC is a Python-based, community-developed BPS software suite with extensive documentation.⁹ COSMIC’s binary evolution is based on BSE, but it has been extensively modified to include updated prescriptions for massive star evolution and binary interactions (see Section 3). All methods needed to generate a population, from initialization to scaling to astrophysical populations, are included in COSMIC.

One of the main features of COSMIC is its ability to *adaptively* determine the size of a simulated binary population

such that it adequately describes the population’s parameter distributions based on the user’s need. However, we note that COSMIC is also able to simulate a population with a predetermined size. All data used to generate a population of binaries, including the parameters of stochastic processes like natal kicks for compact objects, as well as the properties of the population itself, are saved in the output of COSMIC. This allows a user to analyze the entire population, as well as individual interesting systems, from ZAMS all the way to compact object formation. In the subsections below, we outline the process to simulate an astrophysical binary population using COSMIC.

2.1. Fixed Population

The main output from COSMIC is the fixed population, a collection of binary systems that contains enough binaries to capture the underlying shape of the population’s parameter distribution functions resulting from a user-specified SFH and binary evolution model. The fixed population can be convolved with more complex SFHs and scaled to a large number of astrophysical populations. These populations can then be synthetically “observed” and used to explore the variance in synthetic catalogs associated with the simulated binary population and binary evolution model.

The general process to simulate a fixed population is as follows:

1. Select a binary evolution model and SFH.
2. Generate an initial population based on user-selected models for the SFH and initial binary parameter distributions.
3. Evolve the initial population according to the user-specified binary evolution model.
4. If on the first iteration, compare a subset containing half of the simulated population to the total population to determine how closely the binary parameter distributions match one another (we introduce a quantitative “match” condition for making this assessment, described in Section 2.1). If on the second or later iteration, compare the population from the previous iteration to the population containing both the current and previous iterations.
5. If the binary parameter distributions have converged, the population is called the “fixed population,” which contains a large-enough sample to describe the essential statistical features of a binary evolution model.
6. Scale the fixed population to astrophysical populations, weighted either by mass or by number, by sampling the fixed population with replacement.
7. Apply a synthetic observation pipeline to generate a set of synthetic catalogs from the astrophysical populations.

⁹ <https://cosmic-popsynth.github.io/>

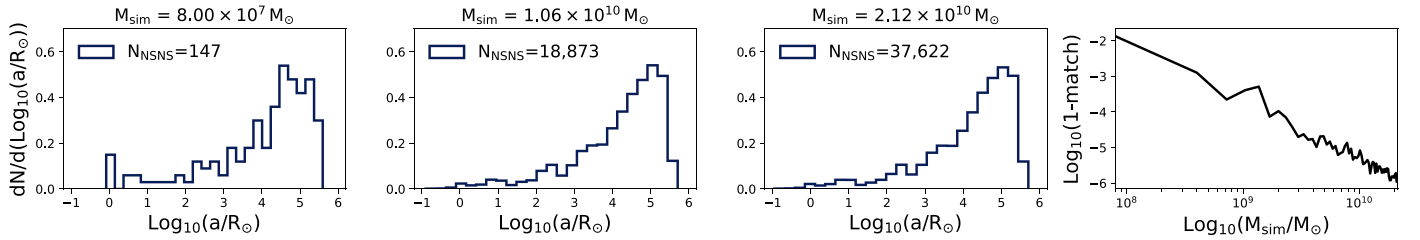


Figure 2. The first three panels show normalized histograms of the semimajor axis at formation for simulated NS + NS populations where each panel includes the population from the previous ones. The fourth panel shows the evolution of the match as the size of the simulated population grows, where we show $\text{Log}_{10}(1\text{-match})$ to illustrate how the match tends to unity.

Figure 1 illustrates the structure and process that COSMIC uses to generate the fixed population. The fixed population is simulated once for each binary evolution model; thus, a study with, for example, 10 binary evolution models will have 10 associated fixed populations. Astrophysical populations can then be sampled from the fixed population, convolved with an SFH, and used to generate a statistical set of synthetic catalogs for each model (i.e., a full study with 10 binary evolution models and one SFH may contain 10,000 synthetic catalogs).

2.1.1. Initializing a Population

The demonstration of COSMIC presented in this paper evolves binary populations using an adapted version of BSE, with several modifications including updated common envelope, wind, and kick prescriptions, which are described further in Section 3. Regardless of the binary evolution model, the fixed population is generated from an initial population of binaries sampled from distribution functions to assign to each binary an initial metallicity (Z), primary mass (m), mass ratio (q), orbital separation (a), eccentricity (e), and birth time (T_0) according to a given SFH. Since binary evolution codes generally evolve a single binary at a time, initial binary populations can be generated using several different star formation histories and distribution functions.

COSMIC is equipped to generate initial populations according to several binary parameter distributions. If the parameters are treated independently, initial masses may be sampled from a Salpeter (1955), Kroupa et al. (1993), or Kroupa (2001) initial mass function (IMF). Mass ratios are uniformly sampled (Mazeh et al. 1992; Goldberg & Mazeh 1994). Orbital separations are sampled log-uniformly, according to Öpik’s law, with lower limits set such that the ZAMS stars do not fill their Roche lobes and with an upper limit of $10^5 R_\odot$ following Dominik et al. (2012). Eccentricities may be sampled from a thermal distribution (Heggie 1975) or uniform distribution (Geller et al. 2019). Binarity can be assumed to have user-specified fractions or the mass-dependent fraction of van Haften et al. (2013). COSMIC is also able to generate initial binary samples following the Moe & di Stefano (2017) multidimensional binary parameter distributions, which include mass- and separation-dependent binary fractions. For easy comparison to previous studies, we use independently distributed parameters with primary masses following the Kroupa et al. (1993) IMF, a thermal eccentricity distribution, and a constant binary fraction of 0.5. For a study of the impact of multidimensional initial distributions on compact object populations, see de Mink & Belczynski (2015) and Klencki et al. (2018).

COSMIC can generate binary populations according to very simple SFH prescriptions. For a more detailed study of the

importance of SFH, see Lamberts et al. (2018). In many cases, it is useful to initially choose a single burst of star formation and later convolve the population with an SFH appropriate for the astrophysical population of interest.

2.1.2. Convergence of Parameter Distributions

There is no formulaic way to a priori predict the required number of binaries to be evolved for a fixed population, because each population depends on a different binary evolution model. The ideal number of simulated systems in a fixed population is such that the population adequately describes the final parameter distribution functions while not simulating so many systems as to be inefficient. To quantify this number, we develop a discrete match criteria, based on the cross ambiguity function, or overlap function, used in matched filtering techniques (e.g., Equation (6) of Chatzioannou et al. 2017).

We use independently generated histograms for each binary parameter, with bin widths determined using Knuth’s rule (Knuth 2006), implemented in ASTROPY (Astropy Collaboration et al. 2013), to track the distribution of each parameter as successive populations are simulated and cumulatively added to the fixed population. Before each histogram is generated, we ensure that similar bin widths are used for each parameter by transforming each set of binary parameters to lie between 0 and 1. We then enforce the physical limits of the simulated systems (e.g., positive definite values for mass and orbital period and eccentricities between 0 and 1) by taking the inverse logistic transform, or logit, which redistributes the transformed data to have limits between $-\text{inf}$ and inf .

We define the match as

$$\text{match} = \frac{\sum_{k=1}^N P_{k,i} P_{k,i+1}}{\sqrt{\sum_{k=1}^N (P_{k,i} P_{k,i}) \sum_{k=1}^N (P_{k,i+1} P_{k,i+1})}}, \quad (1)$$

where $P_{k,i}$ denotes the probability for the k th bin for the i th iteration. The match is limited to values between 0 and 1 and tends to unity as the parameter distributions converge to a distinct shape. The match is specified by the user and can be set to any value. For the study in Section 4, we set $\text{match} \geq 1 - 10^{-5}$ as a fiducial choice, but caution that the results of each simulated population should be carefully checked to confirm that the population does not contain artificial gaps due to low-number statistics in cases of very rare subpopulations.

Figure 2 uses the solar metallicity NS + NS population from Section 4 to illustrate how distributions of the semimajor axis converge to a distinct shape as more binaries are simulated. The evolution of the match (see Equation (1)) as a function of total simulated mass is also shown in terms of $\text{Log}_{10}(1\text{-match})$ to

quantify the convergence of the distributions. As the total simulated mass increases, more NS + NS systems are added to the population, which fills in the normalized distribution and consequently drives the match toward one.

2.2. Generating Astrophysical Population Realizations

Once the fixed population satisfies the user-specified convergence criteria, an astrophysical population can be sampled, and each binary in the astrophysical population can be assigned a position and orientation. The number of sources in each astrophysical population can be calculated by normalizing the size of the fixed population by the ratio of the mass of the astrophysical population to the mass of stars formed to produce the fixed population,

$$N_{\text{astro}} = N_{\text{fixed}} \frac{M_{\text{astro,tot}}}{M_{\text{fixed,stars}}}, \quad (2)$$

or by the ratio of the number of stars in the astrophysical population to the total number of stars formed to produce the fixed population,

$$N_{\text{astro}} = N_{\text{fixed}} \frac{N_{\text{astro,tot}}}{N_{\text{fixed,stars}}}. \quad (3)$$

For each astrophysical realization, N_{astro} binaries are sampled with replacement from the fixed population. These sampled binaries can also be assigned a three-dimensional position and an inclination (i), an argument of periapsis (ω), and a longitude of the ascending node (Ω).

COSMIC allows for several general Galactic position distributions. For the axisymmetric thin and thick disks, the radial and vertical distributions are assumed to be independent. We adopt Galactic position distributions and Galactic component masses from McMillan (2011) for the thin disk, thick disk, and bulge as a fiducial model. However, COSMIC can distribute binaries according to exponential distributions in the radial and vertical directions with any scale height, as well as in spherically symmetric distributions.

Following McMillan (2011), we assume the mass in the thin and thick disks to be $4.32 \times 10^{10} M_{\odot}$ and $1.44 \times 10^{10} M_{\odot}$, respectively, while we assume the mass of the bulge to be $8.9 \times 10^9 M_{\odot}$. Finally, we emphasize that while COSMIC has utility functions implemented to distribute binaries in the Milky Way, the spatial distributions are independent of the binary evolution prescriptions. Thus, multiple spatial distributions can be assumed for a single fixed population, and more sophisticated spatial distribution models can be integrated into future releases of COSMIC.

3. Updates to BSE

COSMIC uses a modified version of BSE to evolve binaries from ZAMS through to compact object formation. We describe several upgrades to binary evolution prescriptions contained in COSMIC below. The version containing these upgrades is fixed as V3.3.0 (Breivik et al. 2020). All future modifications will be openly developed in the COSMIC Github repository.¹⁰

3.1. Winds

Mass loss through stellar winds plays an important role in compact object formation because this determines the mass of the star just before it undergoes a supernova (SN) explosion (e.g., Mapelli et al. 2009; Belczynski et al. 2010; Fryer et al. 2012; Giacobbo et al. 2018). In recent years, models of stellar winds have been revised to reflect updates in our understanding of various relevant physical processes. We have amended the original BSE stellar wind prescriptions with several of these prescriptions, summarized below.

Recent work has shown that line-driven winds exhibit a strong dependence upon metallicity, both on the main sequence (MS) and post-MS (e.g., Vink et al. 2001, 2011; Meynet & Maeder 2005; Gräfener & Hamann 2008). We have updated the original BSE prescription to include metallicity-dependent winds for O and B stars as well as for Wolf-Rayet stars. The winds for O and B stars are treated according to the prescription of Vink et al. (2001), which considers stars with temperatures $12,500 \text{ K} < T_{\text{eff}} < 22,500 \text{ K}$ and $27,500 \text{ K} < T_{\text{eff}} < 50,000 \text{ K}$ separately. As in Rodriguez et al. (2016), we adopt the methods of Dominik et al. (2013), where the high- and low-temperature prescriptions are extended to $T_{\text{eff}} = 25,000 \text{ K}$. Wolf-Rayet star winds are treated according to Vink & de Koter (2005).

Additionally, recent models suggest that as stars approach the limit imposed by the electron-scattering Eddington factor, $\Gamma_e = \chi_e L / (4\pi c G M)$ where χ_e is electron scattering opacity, winds may become insensitive to metallicity (e.g., Gräfener & Hamann 2008; Vink et al. 2011; Chen et al. 2015). Thus, we include Eddington-limited winds using the prescriptions described in Gräfener & Hamann (2008) and Giacobbo et al. (2018).

If the primary star loses mass through a stellar wind, the secondary may accrete some of the ejected material as it orbits through it. The accretion rate onto the secondary can be estimated according to a Bondi-Hoyle type mechanism (Bondi & Hoyle 1944), which is sensitive to the velocity of the wind lost from the primary, $v_w^2 = 2\beta_w GM/R$, where β_w is a constant depending on stellar type (see Equation (9) of Hurley et al. 2002). We have implemented β_w values from Belczynski et al. (2008) and choose this as a default. In this case, β_w is a function of stellar type. For H-rich MS stars, $\beta_w = 0.125$ for masses below $1.4 M_{\odot}$, $\beta_w = 7.0$ for masses above $120 M_{\odot}$, and it is linearly interpolated between. For H-rich giants, $\beta_w = 0.125$ regardless of mass. For He-rich stars, including MS and giants, $\beta_w = 0.125$ for masses below $10 M_{\odot}$, $\beta_w = 7.0$ for masses above $120 M_{\odot}$, and it is linearly interpolated between.

3.2. Mass Transfer Stability and Common Envelope

The stability of Roche-lobe overflow mass transfer is determined through the same process as in Hurley et al. (2002), using critical mass ratios determined from radius-mass exponents (Webbink 1985) where $q_{\text{crit}} = m_{\text{donor}}/m_{\text{accretor}}$. COSMIC allows both models for critical mass ratios for giant star donors detailed in Section 2.6.1 of Hurley et al. (2002). We have added new models that are consistent with binary_c, following Claeys et al. (2014), where we have modified the critical mass ratios of MS/helium-MS stars and binaries with degenerate accretors based on de Mink et al. (2007). For the models that are consistent with Claeys et al. (2014), we adopt the Roche-lobe overflow mass transfer rates in their Equation

¹⁰ <https://github.com/COSMIC-PopSynth/COSMIC>

(10) in the case of stable mass transfer. We have also added a model that is consistent with StarTrack following Belczynski et al. (2008). The most notable difference in the critical mass ratios between StarTrack and BSE or binary_c is the treatment of helium-MS donors where $q_{\text{crit}} = 1.7$ and for helium stars on the Hertzsprung gap or giant branch where $q_{\text{crit}} = 3.5$ based on the findings of Ivanova et al. (2003). Finally, we note that COSMIC allows for user-specified critical mass ratios based on evolutionary stages to allow easy integration with future models as they arise. As a fiducial model for critical mass ratios, we choose the standard model reported in Hurley et al. (2002), which does not differentiate between models for degenerate and nondegenerate accretors.

We employ the standard $\alpha\lambda$ model for common envelope (CE) evolution as done in Hurley et al. (2002). In this case, systems that undergo unstable mass transfer enter into a CE, which can be expelled by the injection of orbital energy from the binary. In this formalism, λ is a factor that determines the binding energy of the envelope to its stellar core, while α is the efficiency factor for injecting orbital energy into the envelope. As with the currently available version of BSE, COSMIC defaults to a variable λ that depends on the evolutionary state of the star following the description in the appendix of Claeys et al. (2014). However, constant λ is also allowed as an option.

As a fiducial CE model, we use the variable binding energy parameter in conjunction with a constant CE efficiency parameter $\alpha = 1.0$ following previous results (e.g., Nelemans et al. 2001a; Dominik et al. 2012). However, previous studies of post-CE binaries point to an efficiency as low as $\alpha = 0.2$ (Zorotovic et al. 2010; Toonen & Nelemans 2013; Camacho et al. 2014). On the other hand, detailed modeling of the CE phase for double NS (DNS) progenitors suggests CE efficiencies may be as high as $\alpha \approx 5$ (Fragos et al. 2019), which may also reduce the tension between rate predictions from CE channels (e.g., Mapelli & Giacobbo 2018) and the empirical DNS merger rate derived from LIGO/Virgo (Abbott et al. 2017).

We also include an option for a “pessimistic CE” scenario, in which unstable mass transfer from a donor star without a well-developed core–envelope structure is always assumed to lead to a merger (Belczynski et al. 2008). This assumption applies to hydrogen-rich and helium stars on the main sequence and Hertzsprung gap, as well as all white dwarfs. When this option is set, we also assume mergers to occur when unstable mass transfer is triggered from donor stars without a clear entropy jump at the core–envelope boundary (Ivanova & Taam 2004), which includes stars on the Hertzsprung gap. Note, however, that the outcomes of CEs in this case are still uncertain (e.g., Deloye & Taam 2010).

Mass transfer involving an evolved He-star donor and a compact object is a critical phase of binary evolution for forming hardened compact binaries that can merge within a Hubble time as GW sources. For progenitors of DNSs, detailed modeling of this phase finds that mass transfer typically proceeds stably (Ivanova et al. 2003; Tauris et al. 2013, 2015) and does not lead to the onset of a CE. Stable mass transfer is also corroborated by studies that compare population modeling to the properties of Galactic DNSs (Vigna-Gómez et al. 2018). Post-mass-transfer separations are typically wider if this phase is modeled stably versus unstably. We allow for the stable mass-transfer evolution of He-star donors with compact object companions to be approximated using the fitting formulae in

Tauris et al. (2015), which can fit for either the post-mass-transfer separation and remaining He-star envelope mass, or just the post-mass-transfer separation.

One important change implemented in COSMIC is the treatment of supernovae that directly follow a CE phase. By default, if a supernova immediately follows a CE (which typically occurs for evolved He-star donors), BSE determines the post-SN barycentric velocity, orbital properties, and survival using the *post-CE* orbital separation and *pre-CE* stellar mass. Therefore, the mass loss in the supernova includes the mass of the donor-star envelope that formed the CE—a self-inconsistent treatment because the ejection of this envelope is used to determine the hardening during the CE phase. This inconsistency leads to artificially amplified mass-loss kicks during the supernova, which are particularly apparent in extremely tight binaries. Therefore, by default, we use the post-CE separation and post-CE mass (which does not include the mass of the envelope) when determining the effect of the subsequent supernova. The effect of this change, particularly on DNS population properties, is explained in more detail in Zevin et al. (2019).

Finally, we note that contact systems can occur if both stellar components overflow their Roche radii or if a stellar component’s radius is larger than the binary’s periastron distance. In this case, a common envelope is always triggered, regardless of the mass transfer stability criteria. This simplification does not allow for long-lived contact binaries, such as W UMa, to be studied in detail, but their formation rates and progenitor populations can be investigated.

3.3. Supernova Explosion Mechanisms and Natal Kicks

3.3.1. Standard Core-collapse Supernovae

Two new prescriptions for the supernova mechanism have been added following Fryer et al. (2012), which are both convection-enhanced and neutrino-driven and account for material falling back onto the compact objects formed in core-collapse SNe. The two cases are delineated by the time between core bounce and explosion, with a “rapid” explosion, which only allows for explosions that occur within 250 ms, and a “delayed” explosion, which allows for longer timescales to explosion. The main difference in these two prescriptions is the presence of a mass gap between NSs and BHs that is produced in the rapid case but is not present in the delayed case.

The inclusion of fallback onto compact objects reduces natal kick magnitudes, due to the fraction of ejected mass during the supernova that falls back onto the compact object. As in the original version of BSE, natal kick magnitudes for standard iron core-collapse supernovae are drawn from a Maxwellian distribution with a dispersion of 265 km s^{-1} , consistent with the proper motions observed for isolated pulsars (Hobbs et al. 2005). The natal kick is then reduced by a factor of $1 - f_{\text{fb}}$, where f_{fb} is the fraction of the ejected supernova mass that will fall back onto the newly formed proto-compact object (see Equations (16) and (19) in Fryer et al. 2012). This efficiently damps the natal kicks for heavy ($M \gtrsim 30 M_{\odot}$) BHs whose progenitors have CO core masses of $M_{\text{CO}} \geq 11 M_{\odot}$. We also include options to allow for no natal kick, full natal kicks (with no reduction due to fallback), and “proportional” kicks that have BH kicks scaled down by a factor of $m_{\text{BH}}/m_{\text{NS}}$, where m_{NS} is the maximum mass of an NS (assumed to be $3.0 M_{\odot}$). An option is also included to scale down the natal kicks for all

BHs by a constant factor. This kick reduction is applied separately and simultaneously to any reduction due to fallback. We note that BHs and NSs are treated as “compact objects” in both BSE and COSMIC, where the difference between the two is chosen by the maximum NS mass.

By default, the natal kick is assumed to impact the proto-compact object in a direction that is isotropically sampled. However, correlations between the proper motions of pulsars and their spin axis suggest that the kick may be preferentially directed along the spin axis of a newly formed compact object (Wang et al. 2006; Ng & Romani 2007; Kaplan et al. 2008). We therefore allow for the kick direction to be constrained within a specified opening angle around the poles of the proto-compact object. Alternatively, the natal kick magnitudes and directions for a binary can be input directly when evolving a binary.

3.3.2. Electron-capture Supernovae

A number of analyses have argued that for stars with main-sequence masses in the range $\sim 8\text{--}11M_{\odot}$, the expected fate is a so-called electron-capture SN (ECSN; e.g., Miyaji et al. 1980; Nomoto 1984, 1987; Podsiadlowski et al. 2004; Ivanova et al. 2008). In this scenario, stars develop helium cores in the range of masses $\sim 1.5\text{--}2.5M_{\odot}$ and never develop an iron core. In this case, collapse is triggered by electron captures onto ^{24}Mg and ^{20}Ne , which lead to a sudden drop of electron pressure support in the stellar core. The collapse occurs when the mass of the stellar core is $>1.38M_{\odot}$ (Miyaji et al. 1980; Nomoto 1984, 1987; Ivanova et al. 2008).

The specific range of helium-core masses expected to give rise to ECSNe is uncertain, and several values have been proposed in the literature. In Hurley et al. (2002), the range $1.6\text{--}2.25M_{\odot}$ was implemented. Podsiadlowski et al. (2004) argued that a broader range of $1.4\text{--}2.5M_{\odot}$ is more realistic. Belczynski et al. (2008) implemented the relatively narrow range of $1.85\text{--}2.25M_{\odot}$, while Andrews et al. (2015) argue that a range of $2\text{--}2.5M_{\odot}$ is required to reproduce the distribution of DNSs in the Milky Way field. Here we have updated the original BSE prescription to allow the lower and upper limits for the helium-core mass range leading to ECSNe to be specified directly. As a default, we follow Podsiadlowski et al. (2004).

In the case of an ECSN, the SN is expected to occur through a prompt (fast) explosion rather than a delayed, neutrino-driven explosion; thus, various analyses have argued that ECSNe likely lead to smaller NS natal kicks relative to core-collapse SNe (e.g., Podsiadlowski et al. 2004; Ivanova et al. 2008). By default, we assume kicks resulting from ECSNe are drawn from a Maxwellian with dispersion velocity $\sigma_{\text{ECSN}} = 20 \text{ km s}^{-1}$, but we include this as a variable to be specified directly by the user.

ECSNe may also occur through accretion-induced collapse (AIC) or merger-induced collapse (MIC). Simple prescriptions are implemented for AIC and MIC in BSE (Hurley et al. 2002). For an ONeMg WD, if it is accreting CO or ONe material from its companion in a binary during Roche lobe overflow, it will undergo AIC (Nomoto & Kondo 1991; Saio & Nomoto 2004) when its mass is larger than the ECSN critical mass. Furthermore, a merger or collision between two CO or ONe WDs leads to an MIC if the mass of the merger/collision product is larger than the ECSN critical mass. Both paths can lead to NS remnants if the mass of the final product is smaller than the maximum NS mass set by BSE.

3.3.3. Ultrastripped Supernovae

For close binaries containing a BH or NS and a Roche-lobe-filling helium star companion, the helium star may be sufficiently stripped of material such that a naked $\sim 1.5M_{\odot}$ core remains (Tauris et al. 2013, 2015). The ensuing explosion of these ultrastripped stars may lead to ejected mass $\lesssim 0.1M_{\odot}$, which may yield natal kick velocities far below those expected for standard core-collapse SNe. Thus, it may be appropriate to draw kicks from a Maxwellian with dispersion width σ smaller than that of the standard Hobbs et al. (2005) distribution ($\sigma = 265 \text{ km s}^{-1}$). Here, whenever a helium star undergoes a CE phase with a compact companion such that a naked helium star forms, we implement the capability of assigning to these objects a smaller natal kick upon collapse and explosion as an ultrastripped SNe.

3.3.4. Pair-instability and Pulsational Pair-instability Supernovae

In the cores of post-carbon-burning stars with sufficiently massive helium cores of $\gtrsim 30M_{\odot}$, photons will readily convert into electron-positron pairs and diminish the pressure support of the core. This will cause the core to rapidly contract and the temperature to increase, allowing for the ignition of carbon, oxygen, or silicon (e.g., Woosley & Heger 2015). For helium-core masses of $\approx 30\text{--}64M_{\odot}$, this spontaneous burning leads to mass ejections, known as pulsational pair instabilities (PPIs; Woosley 2017). These will proceed until the instability is avoided. If the helium-core mass is in the range $\approx 64\text{--}133M_{\odot}$, the instability exceeds the binding energy of the star and the star is completely destroyed, giving a pair-instability supernova (PISN; Woosley 2017).

As our default, we adopt the prescription from Belczynski et al. (2016), which sets the maximum mass of the helium core below which the star is not destroyed by PISN to $45M_{\odot}$ (resulting in a remnant BH mass of $40.5M_{\odot}$, assuming 10% of the mass is lost in the conversion from baryonic to gravitational mass). Helium core masses between 45 and $135M_{\odot}$ lead to the destruction of the star through a PISN, and therefore no remnant formation. We allow for the limiting helium-core mass beyond which a PISN occurs to be set manually to different values.

Alternatively, multiple other prescriptions for determining the (P)PISN mass range and resultant remnant mass are available in COSMIC:

1. Prescription from Spera & Mapelli (2017) (see Appendix B), which is derived from fitting the masses of the compact remnants as a function of the final helium mass fraction and final helium-core mass from the simulations in Woosley (2017).
2. Fit to the grid of simulations from Marchant et al. (2019, see Table 1), which demonstrate a turnover in the relation between presupernova helium-core mass and final mass. Similar to Stevenson et al. (2019), we use a ninth-order polynomial fit to map CO core masses in the range $31.99 \leq M_{\text{He}}/M_{\odot} \leq 61.10$ to BH masses:

$$M_{\text{BH}} = \sum_{l=0}^8 c_l \left(\frac{M_{\text{He}}}{M_{\odot}} \right)^l, \quad (4)$$

where the coefficients are $c_0 = -6.29429263 \times 10^5$, $c_1 = 1.15957797 \times 10^5$, $c_2 = -9.28332577 \times 10^3$, $c_3 = 4.21856189 \times 10^2$, $c_4 = -1.19019565 \times 10^1$,

$c_5 = 2.13499267 \times 10^{-1}$, $c_6 = -2.37814255 \times 10^{-3}$,
 $c_7 = 1.50408118 \times 10^{-5}$, and
 $c_8 = -4.13587235 \times 10^{-8}$.¹¹ The PISN gap, which leaves behind no remnant, is $54.48 < M_{\text{CO}}/M_{\odot} < 113.29$.

3. Fit to the grid of simulations from Woosley (2019, see Table 5), which agree reasonably well with those from Marchant et al. (2019), except that Woosley (2019) find slightly lower helium-core masses undergo PPISN. We again use a ninth-order polynomial fit, mapping CO core masses in the range $29.53 \leq M_{\text{He}}/M_{\odot} \leq 60.12$ to BH masses, with coefficients $c_0 = -3.14610870 \times 10^5$, $c_1 = 6.13699616 \times 10^4$, $c_2 = -5.19249710 \times 10^3$, $c_3 = 2.48914888 \times 10^2$, $c_4 = -7.39487537$, $c_5 = 1.39439936 \times 10^{-1}$, $c_6 = -1.63012111 \times 10^{-3}$, $c_7 = 1.08052344 \times 10^{-5}$, and $c_8 = -3.11019088 \times 10^{-8}$. The PISN gap, which leaves behind no remnant, is $60.12 < M_{\text{CO}}/M_{\odot} < 113.29$.

3.4. Black Hole Spins

We have added new prescriptions for the spins of newly formed BHs from collapsing massive stars. Due to the uncertain values associated with BH natal spins, we allow the spins of all BHs to be set to a specific Kerr value (specified by the user) or drawn from a uniform distribution whose bounds are also user specified. In addition, we have included the prescriptions for BH spin based on the precollapse CO core mass of the progenitor from Belczynski et al. (2020), which result in high spins for low-mass BHs ($\lesssim 30M_{\odot}$, depending on metallicity) and low spins for high-mass BHs.

The latter prescription, based on stellar models computed by the GENEVA stellar evolution code (Eggenberger et al. 2008), assumes that angular momentum is transported in massive stars via meridional currents and is not efficient enough to spin down the core prior to collapse. This is in contrast to newer work (e.g., Fuller & Ma 2019) suggesting that the Taylor–Spruit magnetic dynamo may allow for extremely efficient angular momentum transport through the envelopes of massive stars, producing BHs with dimensionless Kerr spin parameters $a/M \sim 0.01$. We do not include the latter prescription in COSMIC, nor do we allow for the BH spin to be increased by accretion or mergers. These effects will be added in a future release.

3.5. Pulsar Formation and Evolution

We have updated BSE to implement the NS magnetic field and spin period evolution following Kiel et al. (2008) and Ye et al. (2019). All NSs are born with magnetic fields and spin periods that match the observed young pulsars (Manchester et al. 2005); their initial magnetic fields and spin periods are randomly drawn in the range of $10^{11.5} - 10^{15.8}$ G and 30–1000 ms, respectively.

For single NSs or NSs in detached binaries, we assume magnetic dipole radiation for the spin period evolution. The

spin-down rate is calculated by

$$\dot{P} = K \frac{B^2}{P}, \quad (5)$$

where P is the spin period, B is the surface magnetic field, and $K = 9.87 \times 10^{-48} \text{ yr G}^{-2}$. We also assume that the magnetic fields follow exponential decays in a timescale of $\tau = 3 \text{ Gyr}$ (Kiel et al. 2008),

$$B = B_0 \exp\left(\frac{-T}{\tau}\right), \quad (6)$$

where B_0 is the initial magnetic field, and T is the age of the NSs.

On the other hand, binary evolution will affect the NS magnetic fields and spin periods. For NSs in nondetached binaries, their magnetic fields can change significantly during mass accretion on short timescales. We assume “magnetic field burying” (e.g., Bhattacharya & van den Heuvel 1991; Rappaport et al. 1995; Kiel et al. 2008; Tauris et al. 2012) for the magnetic field decay during mass accretion:

$$B = \frac{B_0}{1 + (\Delta M / 10^{-6} M_{\odot})} \exp\left(-\frac{T - t_{\text{acc}}}{\tau}\right). \quad (7)$$

Here, ΔM is the mass accreted, and t_{acc} is the accretion duration. These NSs are spun up according to the amount of angular momentum transferred (Hurley et al. 2002, Equation (54)).

Furthermore, when a neutron star merges with another star (e.g., main-sequence star, giant, or WD) and the final product is an NS, the magnetic field and spin period of this NS are reset by drawing a new magnetic field and spin period from the same initial ranges. If a millisecond pulsar (MSP) is involved in the collision or merger, however, the newly formed NSs are assigned different ranges of initial magnetic fields and spin periods to match those of MSPs, and the newborn NSs will remain MSPs. In this case, the magnetic fields and spin periods are randomly drawn from ranges $10^8 - 10^{8.8}$ G and 3–20 ms, respectively. In addition, we assume a lower limit of 5×10^7 G for the NS magnetic field (Kiel et al. 2008). No lower limit is assumed for the spin periods.

3.6. Stellar Mergers

When two stellar cores spiral in toward one another, the outcome of the subsequent merger depends upon the internal structures (i.e., density profiles) of the two objects. If one of the cores is much denser than the other (for example, if a BH/NS merges with a giant star), a common-envelope-like event ensues. However, if the two stars have comparable compactness (for example, in the case of a roughly equal-mass MS–MS merger), then the merger may result in efficient mixing of the two objects. In either case, the stellar age of the merger product must be specified. Here we adopt the prescriptions of Hurley et al. (2002) to determine outcomes of stellar mergers, with one exception, outlined below.

In the case of an MS–MS merger, we assume the stellar age of the MS merger product is given by

$$t_3 = f_{\text{rejuv}} \frac{t_{\text{MS3}}}{M_3} \left(\frac{M_1 t_1}{t_{\text{MS1}}} + \frac{M_2 t_2}{t_{\text{MS2}}} \right) \quad (8)$$

¹¹ We use different coefficients than in Stevenson et al. (2019) because we find that these are a better fit to data from Marchant et al. (2019) than those originally presented in Stevenson et al. (2019).

where M_1 and M_2 are the masses of the two merger components; $M_3 = M_1 + M_2$ is the mass of the merger product (assuming the stars merge without mass loss; Hurley et al. 2002); t_{MS1} , t_{MS2} , and t_{MS3} are the MS lifetimes of the two merger components and the merger product, respectively; and t_1 and t_2 are the stellar ages of the two merger components at the time of merger. Also, f_{rejuv} is a factor that determines the amount of rejuvenation the merger product experiences through mixing. This factor of course depends upon the internal structure of the two stars, as well as the nature of the merger (i.e., the relative velocity of the two objects at coalescence). In an original BSE, a fixed value of 0.1 is assumed for f_{rejuv} . However, in many instances, this likely leads to overrejuvenation of the merger product. Here we include f_{rejuv} as a free parameter and adopt $f_{\text{rejuv}} = 1$ as our default value.

The outcome of stellar mergers and collisions is expected to play a critical role in dense star clusters where dynamical interactions lead to a pronounced increase in stellar mergers or collisions relative to isolated binaries (e.g., Hills & Day 1976; Bacon et al. 1996; Lombardi et al. 2002; Fregeau & Rasio 2007; Leigh et al. 2011). The details of these merger products have important implications for blue straggler stars (e.g., Sandage 1953; Chatterjee et al. 2013), as well as the formation of massive BHs (e.g., Portegies Zwart & McMillan 2002; Gürkan et al. 2004; Kremer et al. 2020). Thus when modeling stellar and binary evolution in collisional environments like globular clusters, care must be taken when assigning the ages of stars upon collision or merger.

We adopt the merger products from the collision matrix of Hurley et al. (2002, Table 2), but we caution that the unmodified version of BSE contains a typo that causes the merger of two He-MS stars to produce an MS star. The collision matrix covers all merger types, from MS to compact remnants, and depends on the relative compactness of each component star’s core. In the case of WD mergers with companion stars, the WD can mix completely with the stellar core; for example, a merger between a He WD and a star on the first giant branch will produce a giant star with a more massive helium core. If the cores have different compactness, for example, in a merger between a CO WD and a star on the first giant branch, the product will distribute the helium core of the giant around the CO core of the white dwarf, producing an early AGB star. For a detailed discussion of stellar merger products, see Section 2.7.2 of Hurley et al. (2002).

4. Milky Way Population of Compact Binaries

As an illustration of the capabilities of COSMIC, we simulate the Milky Way population of binaries containing combinations of WDs, NSs, and BHs with orbital periods $10 \text{ s} < P_{\text{orb}} < 10^5 \text{ s}$. Several population synthesis investigations using different BPS codes have predicted the population of Galactic compact binaries (e.g., Hils et al. 1990; Tutukov & Yungelson 1992, 1996, 2002; Tutukov et al. 1992; Iben et al. 1995a, 1995b, 1996, 1997; Yungelson et al. 1995, 2006; Nelemans et al. 2001a, 2001b; Fedorova et al. 2004; Ruiter et al. 2010; Liu & Zhang 2014; Korol et al. 2017; Lau et al. 2020). BPS studies have considered the impact of observed space densities (Nissanke et al. 2012) and the effect of different binary evolution models on the observed population (Zorotovic et al. 2010; Dominik et al. 2012; Kremer et al. 2017), or the results of different star formation histories and Galactic spatial

Table 1
Summary of Fixed Population Statistics

Population	$Z (Z_{\odot})$	N_{fixed}	$M_{\text{stars}} (M_{\odot})$
He + He	0.02	1.09×10^5	1.46×10^8
CO + He	0.02	1.76×10^5	1.80×10^8
CO + CO	0.02	1.24×10^6	1.13×10^8
ONe + WD	0.02	1.65×10^5	3.67×10^8
NS + WD	0.02	2.41×10^5	2.22×10^9
BH + WD	0.02	2.05×10^5	1.18×10^{10}
NS + NS	0.02	3.76×10^4	2.12×10^{10}
BH + NS	0.02	6.44×10^4	2.74×10^{10}
BH + BH	0.02	4.62×10^5	1.94×10^{10}
He + He	0.003	2.29×10^5	1.31×10^8
CO + He	0.003	1.93×10^5	1.45×10^8
CO + CO	0.003	1.32×10^6	9.54×10^7
ONe + WD	0.003	2.11×10^5	3.27×10^8
NS + WD	0.003	2.76×10^5	2.37×10^9
BH + WD	0.003	2.12×10^5	1.13×10^{10}
NS + NS	0.003	4.35×10^4	1.55×10^{10}
BH + NS	0.003	6.76×10^4	1.28×10^{10}
BH + BH	0.003	7.58×10^5	1.33×10^{10}

Notes. WD denotes the population containing He, CO, and ONe WDs. N_{fixed} is the size of the fixed population, and M_{stars} is the total mass of the simulated population to produce each fixed subpopulation.

distributions (Yu & Jeffery 2015; Lamberts et al. 2018, 2019) have considered how Galactic compact-object binary populations are affected by different treatments of the binary evolution physics (e.g., common envelope evolution, metallicity-dependent stellar winds), different initial conditions (e.g., stellar IMF, and initial distributions of binary separation and eccentricity), and different assumptions for the Galactic SFH. As a fiducial binary evolution model, we implement several of the updated prescriptions described in Section 3 to be consistent with the models used in Kremer et al. (2019). In particular, we assume that compact objects are formed with the “rapid” model from Fryer et al. (2012) and that BH natal kicks are fallback modulated. We assume that ECSNe follow the Podsiadlowski et al. (2004) prescriptions and do not apply any ultrastripped SNe prescriptions. Unless otherwise noted, we implement the defaults in the original BSE code release as described in Section 3.

As described in Section 2, we simulate a population for each of the Milky Way mass components: the thin and thick disks and the bulge. For the thin disk and the bulge, we generate a fixed population of solar-metallicity binaries from a single burst of star formation that evolves for 13.7 Gyr. Similarly, we generate a fixed population of binaries with 15% solar metallicity from a single burst of star formation that evolves for 13.7 Gyr. We apply an upper orbital period cut of $1000 R_{\odot}$ for systems with a WD or NS primary component because their GW merger time exceeds a Hubble time by several orders of magnitude. The number of binaries simulated in each population for both metallicities and the total mass of all stars formed (including single stars) in the population are detailed in Table 1.

Figure 3 shows the distributions of the masses, semilata recta, and formation times of several combinations of WD, NS, and BH binaries at compact object formation. The solar-metallicity populations (solid lines) follow similar trends when compared to the 15% solar metallicity population, with the

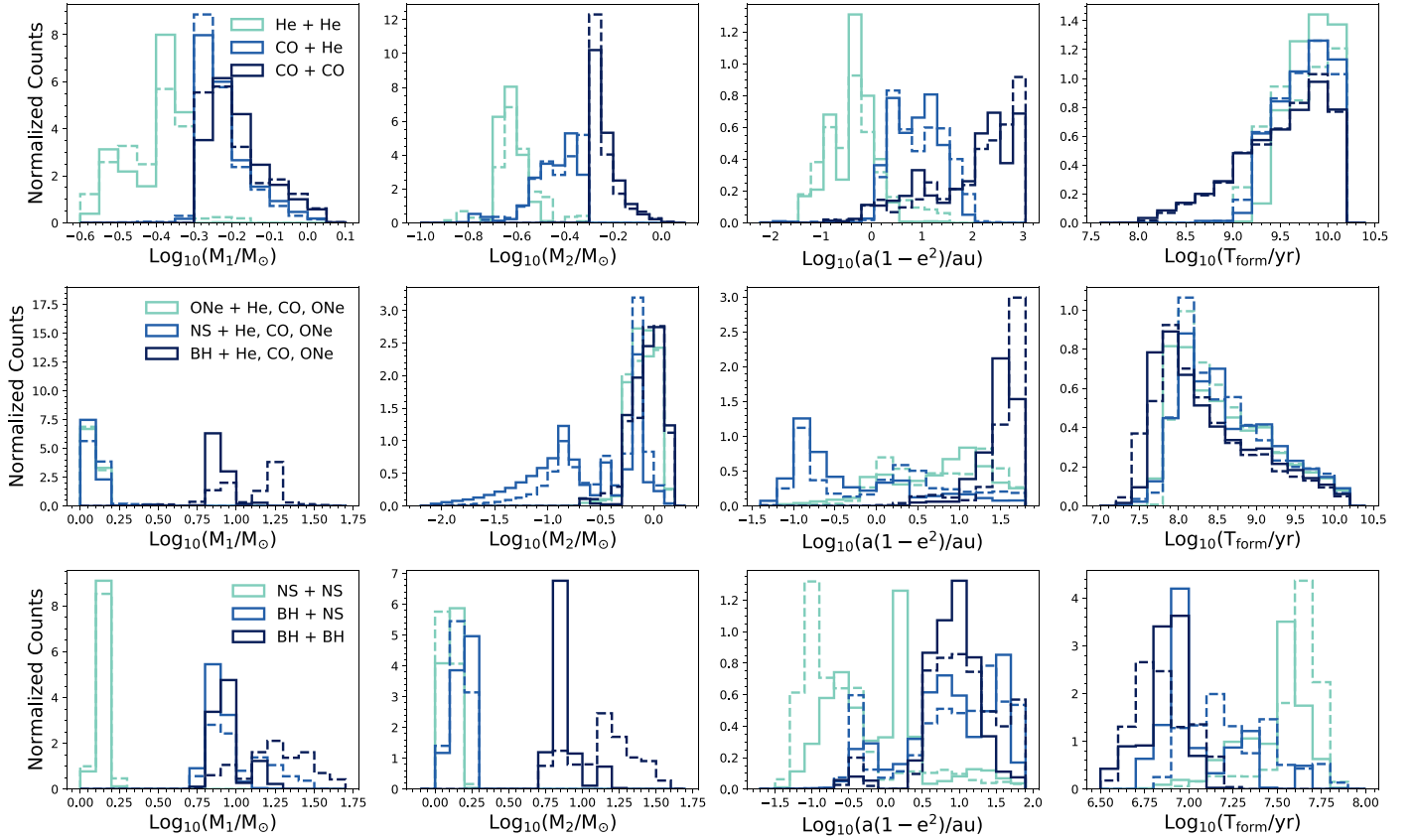


Figure 3. Normalized histograms of the primary mass, secondary mass, semilatus rectum, and formation time of binaries at formation with different combinations of WDs, NSs, and BHs. The WDs are split into separate populations for helium (He), carbon/oxygen (CO), and oxygen/neon (ONe) sources. The solid lines show the formation properties of the solar-metallicity population, while the dashed lines show the 15% solar metallicity population.

exception of the BH populations. This is primarily due to our inclusion of metallicity-dependent stellar winds, which allow for higher mass BHs. Similar to single-star evolution, the formation times of populations with a WD component are longer than those containing NS or BH components, due to decreasing main-sequence lifetimes with increasing progenitor mass.

4.1. Calculation of Signal-to-noise Ratio

The characteristic strain of a GW source, as well as the signal-to-noise ratio (S/N) for a given GW detector, can be calculated in several different approximations, depending upon the properties of the source of interest. Specifically, the most general case of a sky- and polarization-averaged eccentric and chirping source can be approximated if the source is circular or stationary (nonchirping). In this section, we describe the computation of the characteristic strain and LISA S/N in four different regimes: eccentric and chirping, circular and chirping, eccentric and stationary, and circular and stationary.

In the most general case of an eccentric chirping source, the characteristic strain at the n th harmonic can be written as (e.g., Barack & Cutler 2004)

$$h_{c,n}^2 = \frac{1}{(\pi D_L)^2} \left(\frac{2G}{c^3} \frac{\dot{E}_n}{f_n} \right). \quad (9)$$

Here, D_L is the luminosity distance to the source, and f_n is the source-frame GW frequency of the n th harmonic given by $f_n = n f_{\text{orb}}$, where f_{orb} is the source-frame orbital frequency; f_n

is related to the observed (detector frame) GW frequency, $f_{n,d}$, by $f_n = f_{n,d} (1 + z)$.

Here, \dot{E}_n is the time derivative of the energy radiated in GWs at source-frame frequency f_n , which to lowest order is given by (e.g., Peters & Mathews 1963)

$$\dot{E}_n = \frac{32}{5} \frac{G^{7/3}}{c^5} (2\pi f_{\text{orb}} \mathcal{M}_c)^{10/3} g(n, e) \quad (10)$$

where \mathcal{M}_c is the source-frame chirp mass, which is related to detector-frame chirp mass, $\mathcal{M}_{c,d}$, by

$$\mathcal{M}_c = \frac{\mathcal{M}_{c,d}}{1+z} = \frac{(M_1 M_2)^{3/5}}{(M_1 + M_2)^{1/5}} \frac{1}{1+z}. \quad (11)$$

Then $\dot{f}_n = n \dot{f}_{\text{orb}}$ is given by

$$\dot{f}_n = n \frac{96}{10\pi} \frac{(G \mathcal{M}_c)^{5/3}}{c^5} (2\pi f_{\text{orb}})^{11/3} F(e), \quad (12)$$

where $F(e) = [1 + (73/24)e^2 + (37/96)e^4]/(1 - e^2)^{7/2}$. Combining Equations (9), (10), and (12), we obtain the characteristic strain in the detector frame:

$$h_{c,n,d}^2 = \frac{2}{3\pi^{4/3}} \frac{(G \mathcal{M}_c)^{5/3}}{c^3 D_L^2} \frac{1}{f_{n,d}^{1/3} (1+z)^2} \left(\frac{2}{n} \right)^{2/3} \frac{g(n, e)}{F(e)}. \quad (13)$$

For $z \approx 0$, the distinction between the detector-frame and source-frame quantities becomes negligible. In this case, $h_{c,n,d} \approx h_{c,n}$, $f_{n,d} \approx f_n$, and $\mathcal{M}_{c,d} \approx \mathcal{M}_c$, allowing us to write

Table 2
Summary of Milky Way Population Statistics

Component		N_{total}	$S/N > 7$
Thin disk	He + He	3.23×10^7	5053
	CO + He	4.22×10^7	53
	CO + CO	4.75×10^8	1684
	ONe + WD	1.94×10^7	229
	NS + WD	4.69×10^6	240
	BH + WD	7.55×10^5	0
	NS + NS	7.67×10^4	9
	BH + NS	1.02×10^5	15
	BH + BH	1.03×10^6	62
Thick disk	He + He	2.53×10^7	2961
	CO + He	1.92×10^7	10
	CO + CO	2.00×10^8	34
	ONe + WD	9.29×10^6	12
	NS + WD	1.68×10^6	35
	BH + WD	2.71×10^5	0
	NS + NS	4.04×10^4	1
	BH + NS	7.61×10^4	4
	BH + BH	8.22×10^5	4
Bulge	He + He	6.65×10^6	1173
	CO + He	8.70×10^6	2
	CO + CO	9.79×10^7	103
	ONe + WD	4.00×10^6	10
	NS + WD	9.66×10^5	3
	BH + WD	1.56×10^5	0
	NS + NS	1.58×10^4	0
	BH + NS	2.10×10^4	0
	BH + BH	2.12×10^5	6
Total		2.5×10^8	1.17×10^4

Note: WD denotes the population containing He, CO, and ONe WDs.

Equation (13) as

$$h_{c,n}^2 = \frac{2}{3\pi^{4/3}} \frac{(GM_c)^{5/3}}{c^3 D_L^2} \frac{1}{f_n^{1/3}} \left(\frac{2}{n}\right)^{2/3} \frac{g(n, e)}{F(e)}. \quad (14)$$

Henceforth, we ignore dependence on redshift for simplicity, an appropriate approximation because $z \ll 1$ for the Galactic sources of interest in this analysis. For binaries with $e = 0$, all GW power is emitted in the $n = 2$ harmonic. Thus, the characteristic strain for circular and chirping binaries is

$$h_{c,2}^2 = \frac{2}{3\pi^{4/3}} \frac{(GM_c)^{5/3}}{c^3 D_L^2} \frac{1}{f_2^{1/3}}, \quad (15)$$

where we have simply taken $n = 2$ in Equation (14).

For eccentric and stationary sources where $\dot{f} < f/T_{\text{obs}}$, the dimensionless GW strain of the n th harmonic is given by

$$h_n^2 = \frac{128}{5} \frac{(GM_c)^{10/3}}{c^8} \frac{(\pi f_{\text{orb}})^{4/3}}{D_L^2} \frac{g(n, e)}{n^2}. \quad (16)$$

Here we have divided Equation (15) by two times the number of cycles, N , observed for a source within a given frequency bin: $N = f_n^2 / \dot{f}_n$ (see, e.g., Moore et al. 2015). The strain for a stationary and circular source is obtained from Equation (16) and by adopting $n = 2$. The amplitude spectral density (ASD) for a stationary source is

$$\text{ASD}_n = h_n \sqrt{T_{\text{obs}}}, \quad (17)$$

where the power spectral density (PSD) is simply

$$\text{PSD}_n = \text{ASD}_n^2. \quad (18)$$

Having written the expressions for characteristic strain in the four different circular/eccentric and stationary/chirping regimes, we now show how to calculate the LISA S/N. For chirping and eccentric sources, S/N is computed following Smith & Caldwell (2019) as

$$\left(\frac{S}{N}\right)^2 = \sum_{n=1}^{\infty} \int_{f_{\text{start}}}^{f_{\text{end}}} \left[\frac{h_{c,n}(f_n)}{4h_f(f_n)} \right]^2 d \ln f_n, \quad (19)$$

where $h_{c,n}$ is given by Equation (9), and h_f is the characteristic LISA noise curve, which we take from Robson et al. (2019). Here, $f_{\text{start}} = n f_{\text{orb}}$ is the GW frequency emitted at the n th harmonic at the start of the LISA observation, and f_{end} is either the GW frequency at merger or the GW frequency of the n th harmonic of the orbital frequency of the binary at the end of the LISA observation time. The characteristic noise can be expressed as

$$h_f(f_n) = \sqrt{\frac{f_n P_n(f_n)}{\mathcal{R}(f_n)}}, \quad (20)$$

where $P_n(f_n)$ is the noise power spectral density of the detector, and $\mathcal{R}(f_n)$ is the frequency-dependent signal response function.

For a chirping circular source, $h_{c,n}$ in Equation (19) is replaced by $h_{c,2}$ (Equation (15)) so that the S/N is given by

$$\left(\frac{S}{N}\right)^2 = \sum_{n=1}^{\infty} \int_{f_{\text{start}}}^{f_{\text{end}}} \left[\frac{h_{c,2}(f_n)}{4h_f(f_n)} \right]^2 d \ln f_n. \quad (21)$$

For stationary sources, it is no longer necessary to integrate over frequency space. In the stationary and eccentric regime, we obtain

$$\left(\frac{S}{N}\right)^2 \approx \sum_{n=1}^{\infty} \left[\frac{h_n(f_n)}{4h_f(f_n)} \right]^2 f_n T_{\text{obs}}. \quad (22)$$

Finally, for stationary and circular sources, we have

$$\left(\frac{S}{N}\right)^2 \approx \left[\frac{h_2(f)}{4h_f(f)} \right]^2 f T_{\text{obs}}. \quad (23)$$

In the equations above, T_{obs} is the LISA observation time, which we take to be 4 yr. In practice, the vast majority of sources are stationary or can be approximated as stationary because their evolution over the observation time spans less than 500 LISA bins. Based on a 4 yr observation time, this amounts to a frequency change of $\Delta f_{\text{GW}} \lesssim 5 \times 10^{-6}$ Hz and thus has a negligible effect on S/N. In the following section, we assume all sources are stationary.

4.2. An Example Galactic Population of Close WD, NS, and BH Binaries

We convolve the fixed population with the SFHs and spatial distributions described in Section 2 to produce a population of WD, NS, and BH binaries born in the Galaxy. Based on their birth time and the age of each Galactic component, we evolve each binary up to the present and remove all systems that either merge or fill their Roche lobes. Although accreting systems

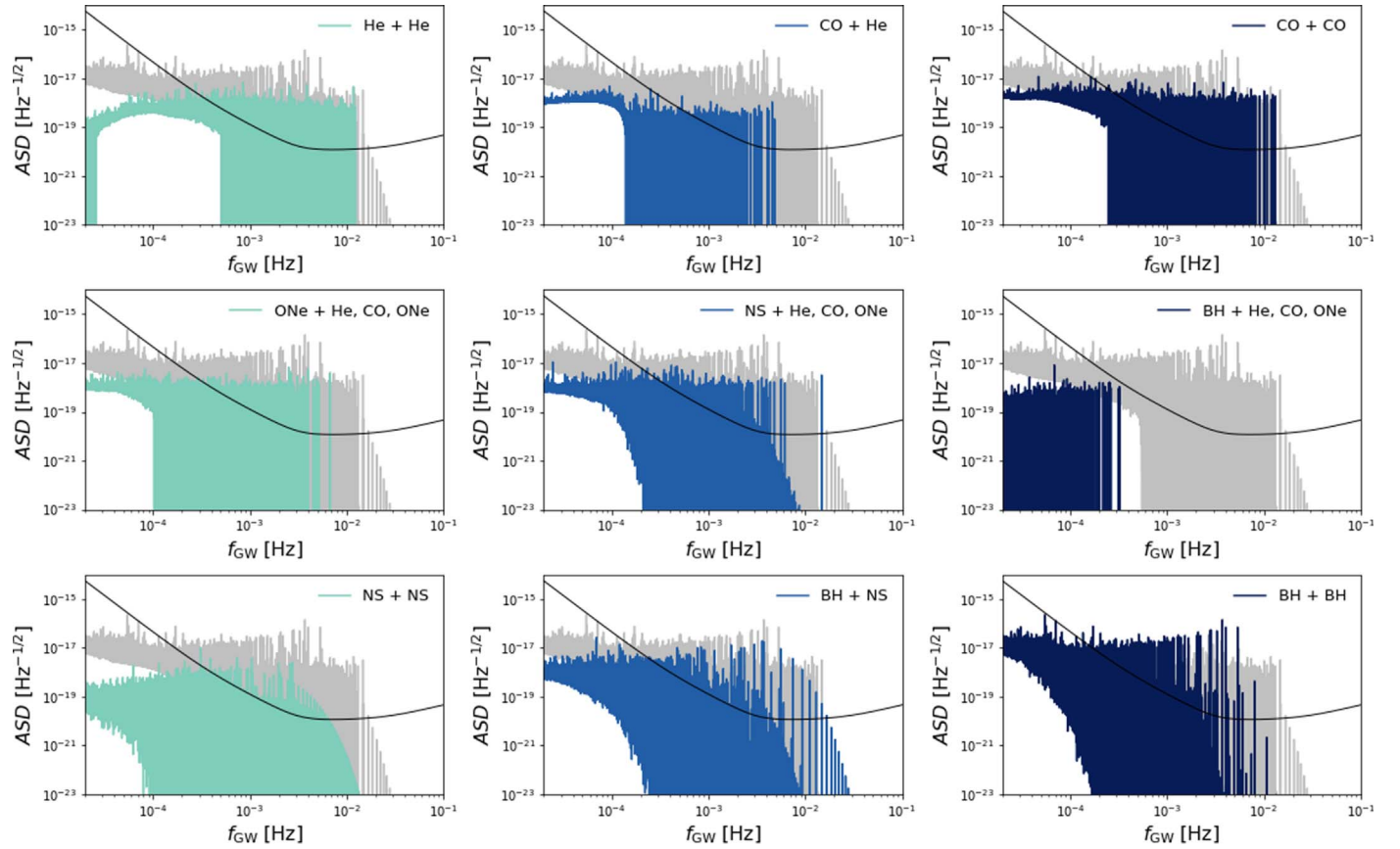


Figure 4. Amplitude spectral density (ASD) as a function of frequency for each population in our Milky Way realization. The gray lines are the same in each plot and show the total ASD from the full population. The black line shows the LISA amplitude spectral density noise floor, without a Galactic foreground contribution.

may also be resolvable GW sources, and indeed may present rich opportunities for studying various aspects of binary evolution (e.g., Kremer et al. 2017; Breivik et al. 2018), we limit this study to only detached sources for simplicity. We note that since one model is used for this example population, the uncertainty across binary evolution models is not well represented. Future studies will investigate, in detail, predicted close binary populations and the uncertainty across several models.

Table 2 shows a summary of the number of sources per population and Milky Way component, as well as the number of systems for which $S/N > 7$ from a Milky Way population realization. Our approach for selecting resolved sources is more simple than the approach used in Korol et al. (2017) and Lamberts et al. (2019). Instead, we apply a running median with a window of 100 frequency bins to the total root power spectral density shown in Figure 4 following Benacquista & Holley-Bockelmann (2006). This produces a synthetic foreground signal similar to that shown in Korol et al. (2017). This foreground is added to the LISA power spectral density curve of Robson et al. (2019) and used to compute the S/N as described in Section 4.1.

The ASD of each population in our Milky Way realization, along with the ASD of the LISA noise floor, is plotted in Figure 4. The vast majority of the signal in the ASD is due to the population of DWDs. The characteristic shape, especially the falloff near 1 mHz, is due to the number of systems radiating GWs in a given frequency bin whose width is determined by LISA’s observing duration as $\sim T_{\text{obs}}^{-1}$. At low frequencies, the number of sources per bin is high, both

because most sources preferentially have longer orbital periods and because the number of bins is low when compared with the number of bins at higher frequencies. As a result, at frequencies in excess of 1 mHz, there is a higher likelihood that a source occupies a unique frequency bin. The features present in the ASD are often smoothed out to produce a foreground (e.g., Littenberg et al. 2013; Korol et al. 2017; Lamberts et al. 2019). Here we present the unsmoothed ASD in order to illustrate the contribution of each population to the signal. The GW signals at harmonics of the orbital frequency are seen in the populations containing an NS or BH due to eccentric sources.

We note that different binary evolution models will produce different ASDs and thus different irreducible foregrounds. This may provide an avenue for distinguishing different binary evolution models. However, we caution that in order to properly determine how well LISA can constrain binary evolution models, resolved sources should be compared to ASDs produced from the same fixed populations. This ensures that self-consistent comparisons are made between different models.

Figure 5 shows the systems resolved with $S/N > 7$ above the irreducible foreground created from the running median of the ASD of the full population. The total number in each Galactic component is listed in Table 2. We find that the vast majority of the population of resolved compact binaries is composed of DWD systems. Our findings are broadly consistent with most previous work that uses population synthesis to predict LISA populations (e.g., Hils et al. 1990; Nelemans et al. 2001b; Ruiter et al. 2010; Yu & Jeffery 2010; Nissanke et al. 2012; Korol et al. 2017; Lamberts et al.

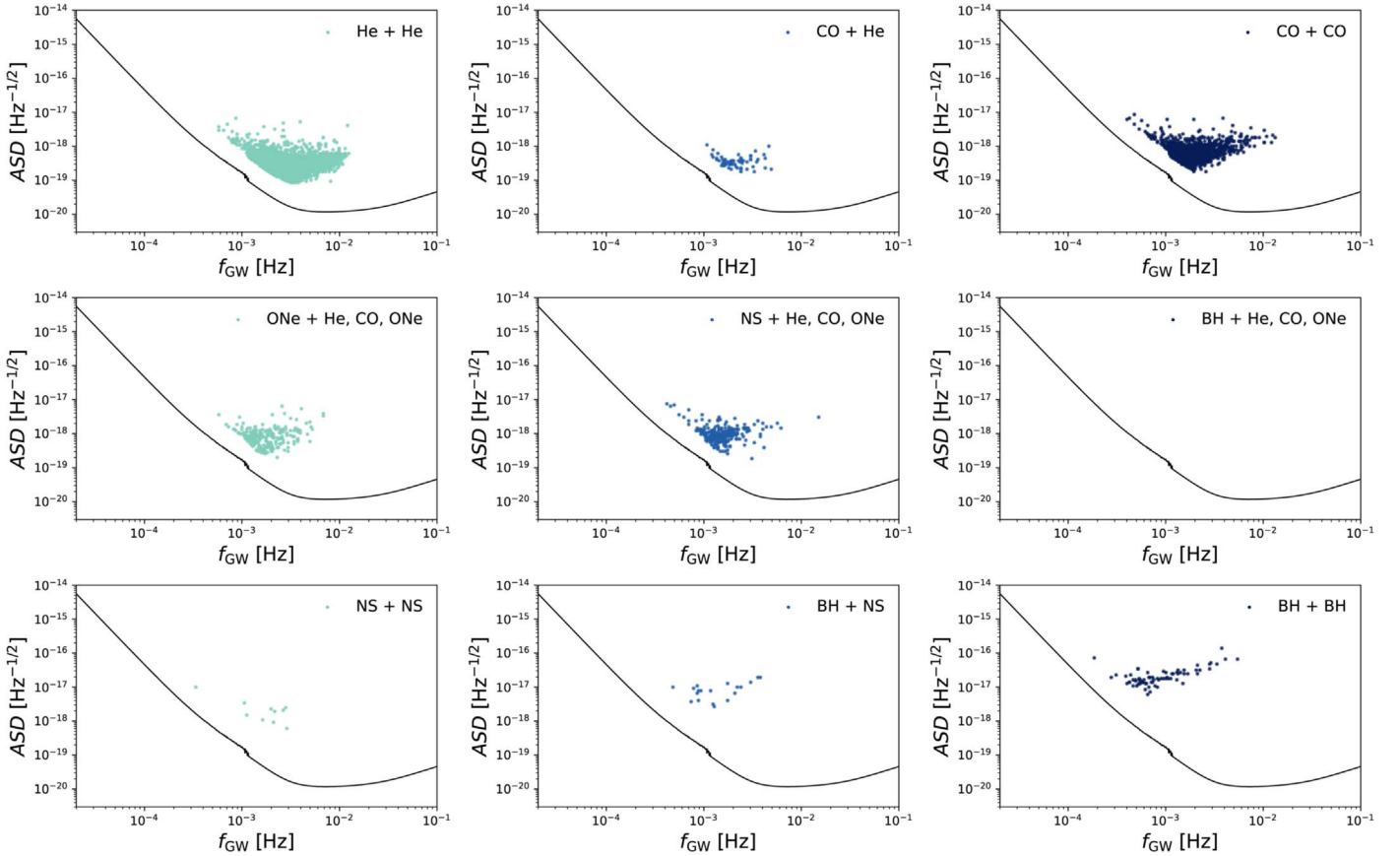


Figure 5. Scatter points of the ASD vs. GW frequency of the systems resolved with $S/N > 7$ for each population in our Milky Way realization. The simulated irreducible foreground and LISA sensitivity are shown in black.

2018, 2019; Lau et al. 2020). We find that the number of resolved DWDs from our simulations is in agreement within a factor of ~ 2 (Nelemans et al. 2001a; Ruiter et al. 2010; Nissanke et al. 2012; Korol et al. 2017; Lamberts et al. 2019). However, we note that we find relatively more He + He than CO + He DWDs than Lamberts et al. (2019). Our resolved DWD population has a factor of ~ 4 smaller DWDs than Yu & Jeffery (2010). We find an order of magnitude more NS + WD binaries than Nelemans et al. (2001a), resulting from updated physics for NS progenitors as described in Section 3.

We find a lower rate of NS + NS binaries detected by LISA than both Lau et al. (2020) and Andrews et al. (2020) by a factor of ~ 3 . The assumptions for both of these studies are different from the model used here. In particular, Lau et al. (2020), following Stevenson et al. (2017) and Vigna-Gómez et al. (2018), assume that the initial distribution of separation is limited to 1000 au, while we place an upper limit of 5000 au. They also use the Fryer et al. (2012) delayed model, instead of the rapid model for compact object formation. Finally, they assume that Roche-lobe overflow from stripped stars onto NSs is stable, which produces more NS + NS binaries at relatively short orbital periods than the model used in this study. The COMPAS $_{\alpha}$, detailed in Stevenson et al. (2017), is the model most similar to the model chosen for this study and results in ~ 10 resolved LISA sources, which is in good agreement with our findings. Andrews et al. (2020) links the NS + NS population resolved by LISA directly to the observed NS + NS merger rates derived from radio observations or LIGO/Virgo. The relative agreement of Andrews et al. (2020) and Lau et al. (2019) suggests that the model chosen for this study does not

reproduce the Milky Way population of NS + NS binaries. Since this study is simply a proof of concept for the capabilities of COSMIC, we leave a careful analysis of the effects of different compact object models as a topic of future study.

Similar to Lamberts et al. (2018), we find relatively few resolved BH + BH binaries even though there are $>10^6$ of them in our total simulated population. This is also true for BH + NS and NS + NS binaries, which are produced at lower rates. The high number of BH binaries relative to NS + NS binaries is due to the relationship between the mass and natal kick of the BHs and NSs at birth. In the Fryer et al. (2012) rapid model, BHs can be formed with a significant amount of fallback and thus reduced natal kicks, which are less likely to unbind the binary. However, BH binaries are mostly unresolved because they tend to occupy frequencies well below 1 mHz. We further note that we use the optimistic assumption that stars that undergo a common envelope on the Hertzsprung gap survive, leading to a larger population.








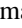

5. Conclusion

We have presented a new, community-developed BPS code, COSMIC, which is adapted from BSE (Hurley et al. 2000, 2002). We have detailed the process COSMIC uses to produce binary populations and shown how to scale these populations to astrophysical realizations by convolving with spatial distributions and an SFH. We have also described several updated prescriptions contained in COSMIC that have strong effects on massive binary populations.

As an illustrative example, we have simulated a Milky Way realization of the thin disk, thick disk, and bulge for all combinations of stellar-remnant binaries potentially observable by LISA. From this example population, we find $\sim 10^8$ stellar-remnant binaries residing in the Galaxy, with $\sim 10^4$ expected to be observed by LISA after a 4 yr observation time, with $S/N > 7$. Future studies will use COSMIC to self-consistently explore the resolved populations of several binary evolution models, as well as Galactic star formation histories and spatial distributions. Such studies that explore the uncertainties across binary evolution models will provide important insights into compact-object populations and their progenitors, allowing comparisons to current and future GW or electromagnetic observations.

The authors are grateful to Vicky Kalogera, who provided invaluable insights during COSMIC's development, Christopher Berry for a careful reading of the manuscript, Alejandro Vigna-Gomez, Tristan Smith, and Robert Caldwell for helpful discussions, and the anonymous referee, whose comments improved the clarity of the manuscript. K.B. acknowledges Sylvia Toonen, Valeriya Korol, Astrid Lamberts, Tassos Fragos, Chris Fryer, and Stephan Justham for helpful conversations about population synthesis and support from the Jeffery L. Bishop Fellowship. J.J.A. acknowledges support by the Danish National Research Foundation (DNRF132). M. K. acknowledges support from the Illinois Space Grant Consortium. F.A.R. acknowledges support from NSF grant AST-1716762 at Northwestern University. The majority of our analysis was performed using the computational resources of the Quest high-performance computing facility at Northwestern University, which is jointly supported by the Office of the Provost, the Office for Research, and Northwestern University Information Technology.

ORCID iDs

Katelyn Breivik  <https://orcid.org/0000-0001-5228-6598>
 Scott Coughlin  <https://orcid.org/0000-0002-0403-4211>
 Michael Zevin  <https://orcid.org/0000-0002-0147-0835>
 Carl L. Rodriguez  <https://orcid.org/0000-0003-4175-8881>
 Kyle Kremer  <https://orcid.org/0000-0002-4086-3180>
 Claire S. Ye  <https://orcid.org/0000-0001-9582-881X>
 Jeff J. Andrews  <https://orcid.org/0000-0001-5261-3923>
 Matthew C. Digman  <https://orcid.org/0000-0003-3815-7065>
 Frederic A. Rasio  <https://orcid.org/0000-0002-7132-418X>

References

- Abbott, B. P., Abbott, R., Abbott, T. D., et al. 2017, *PhRvL*, **119**, 161101
 Abbott, B. P., Abbott, R., Abbott, T. D., et al. 2019, *PhRvX*, **9**, 031040
 Andrews, J. J., Breivik, K., Pankow, C., D'Orazio, D. J., & Safarzadeh, M. 2020, *ApJL*, **892**, L9
 Andrews, J. J., Farr, W. M., Kalogera, V., & Willems, B. 2015, *ApJ*, **801**, 32
 Andrews, J. J., Zezas, A., & Fragos, T. 2018, *ApJS*, **237**, 1
 Astropy Collaboration, Robitaille, T. P., Tollerud, E. J., et al. 2013, *A&A*, **558**, A33
 Bacon, D., Sigurdsson, S., & Davies, M. B. 1996, *MNRAS*, **281**, 830
 Barack, L., & Cutler, C. 2004, *PhRvD*, **69**, 082005
 Barrett, J. W., Gaebel, S. M., Neijssel, C. J., et al. 2018, *MNRAS*, **477**, 4685
 Barrett, J. W., Mandel, I., Neijssel, C. J., Stevenson, S., & Vigna-Gómez, A. 2017, in *IAU Symp. 325, Astroinformatics*, ed. M. Brescia et al. (Cambridge: Cambridge Univ. Press), 46
 Belczynski, K., Bulik, T., Fryer, C. L., et al. 2010, *ApJ*, **714**, 1217
 Belczynski, K., Heger, A., Gladysz, W., et al. 2016, *A&A*, **594**, A97
 Belczynski, K., Kalogera, V., & Bulik, T. 2002, *ApJ*, **572**, 407
 Belczynski, K., Kalogera, V., Rasio, F. A., et al. 2008, *ApJS*, **174**, 223
 Belczynski, K., Klencki, J., Fields, C. E., et al. 2020, *A&A*, **636**, A104
 Benacquista, M., & Holley-Bockelmann, K. 2006, *ApJ*, **645**, 589
 Bhattacharya, D., & van den Heuvel, E. P. J. 1991, *PhR*, **203**, 1
 Bondi, H., & Hoyle, F. 1944, *MNRAS*, **104**, 273
 Breivik, K., Coughlin, S. C., Zevin, M., et al. 2020, COSMIC-PopSynth/COSMIC, V3.3.0: Code release with COSMIC Code release with COSMIC paper: <https://arxiv.org/abs/1911.00903>, Zenodo, doi:10.5281/zenodo.3905335
 Breivik, K., Kremer, K., Bueno, M., et al. 2018, *ApJL*, **854**, L1
 Broekgaarden, F. S., Justham, S., de Mink, S. E., et al. 2019, *MNRAS*, **490**, 5228
 Camacho, J., Torres, S., García-Berro, E., et al. 2014, *A&A*, **566**, A86
 Chatterjee, S., Rasio, F. A., Sills, A., & Glebbeek, E. 2013, *ApJ*, **777**, 106
 Chatziioannou, K., Clark, J. A., Bauswein, A., et al. 2017, *PhRvD*, **96**, 124035
 Chen, Y., Bressan, A., Girardi, L., et al. 2015, *MNRAS*, **452**, 1068
 Claeys, J. S. W., Pols, O. R., Izzard, R. G., Vink, J., & Verbunt, F. W. M. 2014, *A&A*, **563**, A83
 de Donder, E., & Vanbeveren, D. 2004, *NewAR*, **48**, 861
 de Kool, M. 1990, *ApJ*, **358**, 189
 de Mink, S. E., & Belczynski, K. 2015, *ApJ*, **814**, 58
 de Mink, S. E., Pols, O. R., & Hilditch, R. W. 2007, *A&A*, **467**, 1181
 Deloye, C. J., & Taam, R. E. 2010, *ApJL*, **719**, L28
 Dewey, R. J., & Cordes, J. M. 1987, *ApJ*, **321**, 780
 Dominik, M., Belczynski, K., Fryer, C., et al. 2012, *ApJ*, **759**, 52
 Dominik, M., Belczynski, K., Fryer, C., et al. 2013, *ApJ*, **779**, 72
 Eggenberger, P., Meynet, G., Maeder, A., et al. 2008, *Ap&SS*, **316**, 43
 Eldridge, J. J., & Stanway, E. R. 2016, *MNRAS*, **462**, 3302
 Eldridge, J. J., Stanway, E. R., Xiao, L., et al. 2017, *PASA*, **34**, e058
 Fedorova, A. V., Tutukov, A. V., & Yungelson, L. R. 2004, *AsL*, **30**, 73
 Fragos, T., Andrews, J. J., Ramirez-Ruiz, E., et al. 2019, *ApJL*, **883**, L45
 Fregeau, J. M., & Rasio, F. A. 2007, *ApJ*, **658**, 1047
 Fryer, C. L., Belczynski, K., Wiktorowicz, G., et al. 2012, *ApJ*, **749**, 91
 Fuller, J., & Ma, L. 2019, *ApJL*, **881**, L1
 Geller, A. M., Leigh, N. W. C., Giersz, M., Kremer, K., & Rasio, F. A. 2019, *ApJ*, **872**, 165
 Giacobbo, N., & Mapelli, M. 2018, *MNRAS*, **480**, 2011
 Giacobbo, N., Mapelli, M., & Spera, M. 2018, *MNRAS*, **474**, 2959
 Goldberg, D., & Mazeh, T. 1994, *A&A*, **282**, 801
 Gräfener, G., & Hamann, W. R. 2008, *A&A*, **482**, 945
 Gürkan, M. A., Freitag, M., & Rasio, F. A. 2004, *ApJ*, **604**, 632
 Heggie, D. C. 1975, *MNRAS*, **173**, 729
 Hills, J. G., & Day, C. A. 1976, *Astrophys. Lett.*, **17**, 87
 Hils, D., Bender, P. L., & Webbink, R. F. 1990, *ApJ*, **360**, 75
 Hobbs, G., Lorimer, D. R., Lyne, A. G., & Kramer, M. 2005, *MNRAS*, **360**, 974
 Hurley, J. R., Pols, O. R., & Tout, C. A. 2000, *MNRAS*, **315**, 543
 Hurley, J. R., Tout, C. A., & Pols, O. R. 2002, *MNRAS*, **329**, 897
 Iben, I. J., Tutukov, A. V., & Yungelson, L. R. 1995a, *ApJS*, **100**, 217
 Iben, I. J., Tutukov, A. V., & Yungelson, L. R. 1995b, *ApJS*, **100**, 233
 Iben, I. J., Tutukov, A. V., & Yungelson, L. R. 1996, *ApJ*, **456**, 750
 Iben, I. J., Tutukov, A. V., & Yungelson, L. R. 1997, *ApJ*, **475**, 291
 Ivanova, N., Belczynski, K., Kalogera, V., Rasio, F. A., & Taam, R. E. 2003, *ApJ*, **592**, 475
 Ivanova, N., Heinke, C. O., Rasio, F. A., Belczynski, K., & Fregeau, J. M. 2008, *MNRAS*, **386**, 553
 Ivanova, N., & Taam, R. E. 2004, *ApJ*, **601**, 1058
 Izzard, R. G., Dray, L. M., Karakas, A. I., Lugaro, M., & Tout, C. A. 2006, *A&A*, **460**, 565
 Izzard, R. G., Glebbeek, E., Stancliffe, R. J., & Pols, O. R. 2009, *A&A*, **508**, 1359
 Izzard, R. G., Tout, C. A., Karakas, A. I., & Pols, O. R. 2004, *MNRAS*, **350**, 407
 Kaplan, D. L., Chatterjee, S., Gaensler, B. M., & Anderson, J. 2008, *ApJ*, **677**, 1201
 Kiel, P. D., Hurley, J. R., Bailes, M., & Murray, J. R. 2008, *MNRAS*, **388**, 393
 Klencki, J., Moe, M., Gladysz, W., et al. 2018, *A&A*, **619**, A77
 Knuth, K. H. 2006, arXiv:physics/0605197
 Korol, V., Rossi, E. M., Groot, P. J., et al. 2017, *MNRAS*, **470**, 1894
 Kremer, K., Breivik, K., Larson, S. L., & Kalogera, V. 2017, *ApJ*, **846**, 95
 Kremer, K., Rodriguez, C. L., Amaro-Seoane, P., et al. 2019, *PhRvD*, **99**, 063003
 Kremer, K., Ye, C. S., Rui, N. Z., et al. 2020, *ApJS*, **247**, 48
 Kroupa, P. 2001, *MNRAS*, **322**, 231
 Kroupa, P., Tout, C. A., & Gilmore, G. 1993, *MNRAS*, **262**, 545

- Kruckow, M. U., Tauris, T. M., Langer, N., Kramer, M., & Izzard, R. G. 2018, *MNRAS*, **481**, 1908
- Lamberts, A., Blunt, S., Littenberg, T. B., et al. 2019, *MNRAS*, **490**, 2426
- Lamberts, A., Garrison-Kimmel, S., Hopkins, P., et al. 2018, *MNRAS*, **480**, 2704
- Lau, M. Y. M., Mandel, I., Vigna-Gómez, A., et al. 2020, *MNRAS*, **492**, 3061
- Leigh, N., Sills, A., & Knigge, C. 2011, *MNRAS*, **416**, 1410
- Lipunov, V. M., Ozernoy, L. M., Popov, S. B., Postnov, K. A., & Prokhorov, M. E. 1996a, *ApJ*, **466**, 234
- Lipunov, V. M., & Postnov, K. A. 1987, *SvA*, **31**, 228
- Lipunov, V. M., Postnov, K. A., & Prokhorov, M. E. 1996b, *A&A*, **310**, 489
- Lipunov, V. M., Postnov, K. A., Prokhorov, M. E., & Bogomazov, A. I. 2009, *ARep*, **53**, 915
- Littenberg, T. B., Larson, S. L., Nelemans, G., & Cornish, N. J. 2013, *MNRAS*, **429**, 2361
- Liu, J., & Zhang, Y. 2014, *PASP*, **126**, 211
- Lombardi, J. C. J., Warren, J. S., Rasio, F. A., Sills, A., & Warren, A. R. 2002, *ApJ*, **568**, 939
- Manchester, R. N., Hobbs, G. B., Teoh, A., & Hobbs, M. 2005, *AJ*, **129**, 1993
- Mapelli, M., Colpi, M., & Zampieri, L. 2009, *MNRAS*, **395**, L71
- Mapelli, M., & Giacobbo, N. 2018, *MNRAS*, **479**, 4391
- Marchant, P., Renzo, M., Farmer, R., et al. 2019, *ApJ*, **882**, 36
- Mazeh, T., Goldberg, D., Duquennoy, A., & Mayor, M. 1992, *ApJ*, **401**, 265
- McMillan, P. J. 2011, *MNRAS*, **414**, 2446
- Meynet, G., & Maeder, A. 2005, *A&A*, **429**, 581
- Miyaji, S., Nomoto, K., Yokoi, K., & Sugimoto, D. 1980, *PASJ*, **32**, 303
- Moe, M., & di Stefano, R. 2017, *ApJS*, **230**, 15
- Moore, C. J., Cole, R. H., & Berry, C. P. L. 2015, *CQGra*, **32**, 015014
- Nelemans, G., Portegies Zwart, S. F., Verbunt, F., & Yungelson, L. R. 2001a, *A&A*, **365**, 491
- Nelemans, G., Yungelson, L. R., & Zwart, S. F. P. 2001b, *A&A*, **375**, 890
- Nelson, C. A., & Eggleton, P. P. 2001, *ApJ*, **552**, 664
- Ng, C.-Y., & Romani, R. W. 2007, *ApJ*, **660**, 1357
- Nissanke, S., Vallisneri, M., Nelemans, G., & Prince, T. A. 2012, *ApJ*, **758**, 131
- Nomoto, K. 1984, *ApJ*, **277**, 791
- Nomoto, K. 1987, *ApJ*, **322**, 206
- Nomoto, K., & Kondo, Y. 1991, *ApJL*, **367**, L19
- Paxton, B., Bildsten, L., Dotter, A., et al. 2011, *ApJS*, **192**, 3
- Paxton, B., Cantiello, M., Arras, P., et al. 2013, *ApJS*, **208**, 4
- Paxton, B., Marchant, P., Schwab, J., et al. 2015, *ApJS*, **220**, 15
- Paxton, B., Schwab, J., Bauer, E. B., et al. 2018, *ApJS*, **234**, 34
- Paxton, B., Smolec, R., Schwab, J., et al. 2019, *ApJS*, **243**, 10
- Peters, P. C., & Mathews, J. 1963, *PhRv*, **131**, 435
- Podsiadlowski, P., Langer, N., Poelarends, A. J. T., et al. 2004, *ApJ*, **612**, 1044
- Pols, O. R., Schröder, K.-P., Hurley, J. R., Tout, C. A., & Eggleton, P. P. 1998, *MNRAS*, **298**, 525
- Pols, O. R., Tout, C. A., Eggleton, P. P., & Han, Z. 1995, *MNRAS*, **274**, 964
- Portegies Zwart, S. F., & McMillan, S. L. W. 2002, *ApJ*, **576**, 899
- Portegies Zwart, S. F., & Verbunt, F. 1996, *A&A*, **309**, 179
- Price-Whelan, A., Breivik, K., D'Orazio, D., et al. 2019, *BAAS*, **51**, 206
- Rappaport, S., Podsiadlowski, P., Joss, P. C., di Stefano, R., & Han, Z. 1995, *MNRAS*, **273**, 731
- Ritter, H., Politano, M., Livio, M., & Webbink, R. F. 1991, *ApJ*, **376**, 177
- Robson, T., Cornish, N. J., & Liu, C. 2019, *CQGra*, **36**, 105011
- Rodriguez, C. L., Chatterjee, S., & Rasio, F. A. 2016, *PhRvD*, **93**, 084029
- Ruiter, A. J., Belczynski, K., Benacquista, M., Larson, S. L., & Williams, G. 2010, *ApJ*, **717**, 1006
- Saio, H., & Nomoto, K. 2004, *ApJ*, **615**, 444
- Salpeter, E. E. 1955, *ApJ*, **121**, 161
- Sandage, A. R. 1953, *AJ*, **58**, 61
- Siess, L., Izzard, R. G., Davis, P. J., & Deschamps, R. 2013, *A&A*, **550**, A100
- Smith, T. L., & Caldwell, R. R. 2019, *PhRvD*, **100**, 104055
- Spera, M., & Mapelli, M. 2017, *MNRAS*, **470**, 4739
- Spera, M., Mapelli, M., & Bressan, A. 2015, *MNRAS*, **451**, 4086
- Spera, M., Mapelli, M., Giacobbo, N., et al. 2019, *MNRAS*, **485**, 889
- Stanway, E. R., & Eldridge, J. J. 2018, *MNRAS*, **479**, 75
- Stanway, E. R., Eldridge, J. J., & Becker, G. D. 2016, *MNRAS*, **456**, 485
- Stevenson, S., Berry, C. P. L., & Mandel, I. 2017, *MNRAS*, **471**, 2801
- Stevenson, S., Sampson, M., Powell, J., et al. 2019, *ApJ*, **882**, 121
- Tauris, T. M., Langer, N., & Kramer, M. 2012, *MNRAS*, **425**, 1601
- Tauris, T. M., Langer, N., Moriya, T. J., et al. 2013, *ApJL*, **778**, L23
- Tauris, T. M., Langer, N., & Podsiadlowski, P. 2015, *MNRAS*, **451**, 2123
- Taylor, S. R., & Gerosa, D. 2018, *PhRvD*, **98**, 083017
- Toonen, S., Claeys, J. S. W., Mennekens, N., & Ruiter, A. J. 2014, *A&A*, **562**, A14
- Toonen, S., & Nelemans, G. 2013, *A&A*, **557**, A87
- Toonen, S., Nelemans, G., & Portegies Zwart, S. 2012, *A&A*, **546**, A70
- Tutukov, A., & Yungelson, L. 1996, *MNRAS*, **280**, 1035
- Tutukov, A. V., & Yungelson, L. R. 1992, *SvA*, **36**, 266
- Tutukov, A. V., & Yungelson, L. R. 2002, *ARep*, **46**, 667
- Tutukov, A. V., Yungelson, L. R., & Iben, I. J. 1992, *ApJ*, **386**, 197
- van Haaften, L. M., Nelemans, G., Voss, R., et al. 2013, *A&A*, **552**, A69
- Vigna-Gómez, A., Neijssel, C. J., Stevenson, S., et al. 2018, *MNRAS*, **481**, 4009
- Vink, J. S., & de Koter, A. 2005, *A&A*, **442**, 587
- Vink, J. S., de Koter, A., & Lamers, H. J. G. L. M. 2001, *A&A*, **369**, 574
- Vink, J. S., Muijres, L. E., Anthonisse, B., et al. 2011, *A&A*, **531**, A132
- Wang, C., Lai, D., & Han, J. L. 2006, *ApJ*, **639**, 1007
- Webbink, R. F. 1985, in *Stellar Evolution and Binaries*, ed. J. E. Pringle & R. A. Wade (Cambridge: Cambridge Univ. Press), 39
- Whyte, C. A., & Eggleton, P. P. 1985, *MNRAS*, **214**, 357
- Woosley, S. E. 2017, *ApJ*, **836**, 244
- Woosley, S. E. 2019, *ApJ*, **878**, 49
- Woosley, S. E., & Heger, A. 2015, in *Very Massive Stars in the Local Universe*, ed. J. S. Vink, 199
- Ye, C. S., Kremer, K., Chatterjee, S., Rodriguez, C. L., & Rasio, F. A. 2019, *ApJ*, **877**, 122
- Yu, S., & Jeffery, C. S. 2010, *A&A*, **521**, A85
- Yu, S., & Jeffery, C. S. 2015, *MNRAS*, **448**, 1078
- Yungelson, L., Livio, M., Tutukov, A., & Kenyon, S. J. 1995, *ApJ*, **447**, 656
- Yungelson, L. R., Lasota, J. P., Nelemans, G., et al. 2006, *A&A*, **454**, 559
- Zevin, M., Kremer, K., Siegel, D. M., et al. 2019, *ApJ*, **886**, 4
- Zorotovic, M., Schreiber, M. R., Gänsicke, B. T., & Nebot Gómez-Morán, A. 2010, *A&A*, **520**, A86